# Magnetic Vortex States in Small Octahedral Particles of Intermediate Titanomagnetite

Geochemistry, Geophysics, Geosystems

RESEARCH ARTICLE
10.1029/2018GC007723

# Magnetic Vortex States in Small Octahedral Particles of Intermediate Titanomagnetite

E. Khakhalova[1], B. M. Moskowitz[1], W. Williams[2], A. R. Biedermann[1,3], and P. Solheid[1]

[1]Institute for Rock Magnetism, Department of Earth Sciences, University of Minnesota, Minneapolis, MN, USA, [2]Department of Geosciences, University of Edinburgh, Edinburgh, UK, [3]Institute of Geophysics, ETH Zurich, Zurich, Switzerland

**Key Points:**
- Magnetic vortex states were observed using magnetic force microscopy in micron-sized grains of intermediate titanomagnetite
- Magnetic imaging agrees well with micromagnetic modeling showing single-vortex and multivortex states
- Crystallographic data from electron backscatter diffraction combined with micromagnetic modeling are critical for MFM interpretation

**Supporting Information:**
- Supporting Information S1
- Data Set S1

**Correspondence to:**
E. Khakhalova,
khakh001@umn.edu

**Citation:**
Khakhalova, E., Moskowitz, B. M., Williams, W., Biedermann, A. R., & Solheid, P. (2018). Magnetic vortex states in small octahedral particles of intermediate titanomagnetite. *Geochemistry, Geophysics, Geosystems*, *19*. https://doi.org/10.1029/2018GC007723

Received 31 MAY 2018
Accepted 13 AUG 2018
Accepted article online 20 AUG 2018



**Abstract** Fine particles of titanomagnetites ($Fe_{3-x}Ti_xO_4$, $x > 0.5$) in the pseudo-single-domain (PSD) size (0.5–20 μm) are important carriers of natural remanent magnetization in basalts. Understanding the mechanism of magnetic recording in these grains has important implications for paleomagnetic studies. This study reports first observations of magnetic vortex states in intermediate titanomagnetite. We imaged magnetic structures of 109 synthetic titanomagnetite grains with x = 0.54 (TM54) and 1–4-μm size using magnetic force microscopy. For six grains, we explored local energy minimum states after alternating field demagnetization and saturation isothermal remanent magnetization. According to the magnetic force microscopy results, 80% of TM54 grains display in-plane magnetization with one to four domains, vortex-like or flux-closure structures, and Néel-like domain walls. Electron backscatter diffraction data on six grains showed that their surface orientations are cutting planes of octahedral crystals and those with approximately square cross sections are within 15° of a (100) crystallographic plane. Magnetic force microscopy observations of magnetic structures in ~1.5-μm grains agree well with numerical micromagnetic modeling of a pyramidal shaped grain with a (100) square base and displayed four discrete local energy minimum states: a single vortex as a ground state and three multivortex states with higher energy. Our observations show that vortex states in titanomagnetite grains (1–5 μm) occur at the lower end of the PSD size range in this mineral and corresponding to a size range known to carry stable and reliable remanence in natural titanomagnetites.

## 1. Introduction

Titanium-rich titanomagnetites ($Fe_{3-x}Ti_xO_4$, $x > 0.5$) and their oxidized equivalents are the main source of magnetic records in submarine basalts and play an important role in paleomagnetism. Fine particles of titanomagnetite in single-domain (SD) or pseudo-single-domain (PSD) states (0.5–20 μm in size) are the dominant carriers of natural remanent magnetization in these rocks. Yet the mechanism of magnetic recording in PSD grains is not completely understood (e.g., Dunlop & Özdemir, 1997; Fabian & Hubert, 1999; Nagy et al., 2017; Roberts et al., 2017).

A PSD state has traditionally been described as a transitional state from SD with uniform magnetization to a true multidomain (MD) state with well-defined magnetic domains and bulk domain walls (Bloch walls). Hard magnetic materials with dominant magnetocrystalline anisotropy ($K_1$) can display more abrupt transitions from SD to MD states. In contrast, soft magnetic materials with low magnetocrystalline anisotropy (such as magnetite and titanomagnetite) display a range of grain sizes with PSD states (Rave et al., 1998). These states are characterized by continuous magnetization states emerging as vortices, curls, and flux-closure structures as shown by numerical micromagnetic models (e.g., Nagy et al., 2017; Rave et al., 1998; Williams et al., 2006; Williams & Wright, 1998).

According to recent micromagnetic calculations in magnetite, single-vortex states can carry an extremely stable and reliable remanence over billions of years (Nagy et al., 2017). Vortex states, which are predicted to occur just above the SD size range, have been observed in ~200-nm magnetite grains using electron holography (Almeida et al., 2014, 2016; Kimura et al., 2013). For titanomagnetite, the size range between SD to multidomain states depends on Ti content, and for titanomagnetite with x = 0.6 (TM60), it is estimated to be ~0.16 to 3 μm (Butler & Banerjee, 1975; Rave et al., 1998; Soffel, 1971). Even though this range includes larger grain sizes than in magnetite (0.08–1 μm), there is no high-resolution domain observation study for small PSD grains (<5 μm) of intermediate titanomagnetite. Direct observation of vortex states in these grains can provide insights on how they carry remanence and provide constrains for micromagnetic models which has important consequences for paleomagnetic studies.

Previous domain observations on intermediate titanomagnetite were conducted mainly on larger titanomagnetite grains (>5 μm) using low-resolution optical techniques (Ambatiello & Soffel, 1996; Geiß et al., 1996; Halgedahl, 1987; Halgedahl & Fuller, 1980, 1983; Hoffmann et al., 1987; Soffel, 1977; Soffel et al., 1990), the dried-Bitter method and scanning electron microscopy (Moskowitz et al., 1988), or magnetic force micrscopy (De Groot et al., 2014). These observations showed that domain patterns in titanomagnetite can be complex and similar to those observed in materials with uniaxial anisotropy, and unlike those expected for materials with cubic magnetocrystalline anisotropy, such as titanomagnetite. The source of the uniaxial anisotropy in titanomagnetite was assumed to be controlled by stress due to their high magnetostriction relative to magnetocrystalline anisotropy (e.g., Appel, 1987; Appel & Soffel, 1984; Fabian, 2006; Halgedahl, 1987; Hodych & Matzka, 2004; Moskowitz et al., 1988). However, Gee and Kent (1995), using hysteresis data from a suite of young mid-ocean ridge basalts containing ~TM60, argued that cubic magnetocrystalline anisotropy was the dominant form for at least the SD-sized fraction of grains in their samples (see also Mitra et al., 2011).On the other hand, Fabian (2006, 2012) in a more detailed analysis of mid-ocean ridge basalt hysteresis data using the approach to saturation in high fields of 7 T and several other lines of evidence concluded that anisotropy in intermediate titanomagnetite (>TM50) is best explained by uniaxial stress anisotropy rather than multiaxial cubic anisotropy.

This study focuses on the direct domain observations of titanomagnetite with grain size 1–4 μm using magnetic force microscopy (MFM). This technique has been used to image magnetic features on submicron scales in magnetite and titanomagnetite (De Groot et al., 2014; Foss et al., 1998; Krása et al., 2005; Muxworthy & Williams, 2006; Pan et al., 2002; Pokhil & Moskowitz, 1996), in silicate-hosted magnetic inclusions (Feinberg et al., 2005; Frandsen et al., 2004), and in magnetic dendrites in archeological slag and basaltic glass (Shaar & Feinberg, 2013).

Using MFM, we imaged magnetic microstructures of 109 equidimensional titanomagnetite grains with x = 0.54 (TM54). For six grains, we explored local energy minimum (LEM) states after alternating field demagnetization (AFD) and saturation isothermal remanent magnetization (SIRM). Since MFM is sensitive only to the near surface stray fields from the magnetization of a three-dimensional domain structure, the interpretation of the actual domain structure is difficult without additional information about the surface plane crystallographic orientation and from three-dimensional micromagnetic modeling. Thus, to better interpret observed magnetic structures, we obtained crystallographic orientations of six grains using electron backscatter diffraction (EBSD). Finally, we compared experimental results with micromagnetic modeling of titanomagnetite using the software package MERRIL (Ó Conbhuí et al., 2018) to visualize possible magnetic structures in 3-D.

## 2. Materials and Methods

### 2.1. Sample Preparation and Magnetic Characterization

Titanomagnetite grains were synthesized using the glass–ceramic method (Worm & Markert, 1987) with a few modifications (see supporting information S1; Dahlberg & Zhu, 1995; Jackson & Solheid, 2010). The sample contained nonoriented titanomagnetite grains dispersed in a nonmagnetic glassy silicate matrix (Figure 1). High-temperature magnetization measurements (M-T) showed nearly reversible heating and cooling curves with a single Curie temperature of 215 °C. The Curie temperature indicates a composition of x = 0.54 or TM54 (e.g., Lattard et al., 2006). Bulk magnetic properties of the sample can be found in supporting information. However, the bulk sample contains a much broader range in grain sizes and shapes than the subset of grains imaged with the MFM.

Prior to magnetic imaging and characterization by electron microscopy, the sample was mounted in epoxy and mechanically polished using diamond compounds. This step was followed by a chemical polishing with amorphous silica to obtain a smooth surface and to reduce the surface stress induced by mechanical polishing.

### 2.2. Scanning Electron Microscopy

Scanning electron microscopy (SEM) and electron backscatter diffraction (EBSD) was performed on a Scanning Electron Microscope JEOL 6500 at the Characterization Facility at the University of Minnesota. Titanomagnetite composition was determined from point spectra on 20 randomly chosen grains using energy-dispersive X-ray spectroscopy (EDS). Interpretation of the SEM-EDS data was based on elemental ratios (Fe/Ti) rather than absolute concentrations. The Fe/Ti ratios yielded a composition x = 0.52–0.54 with

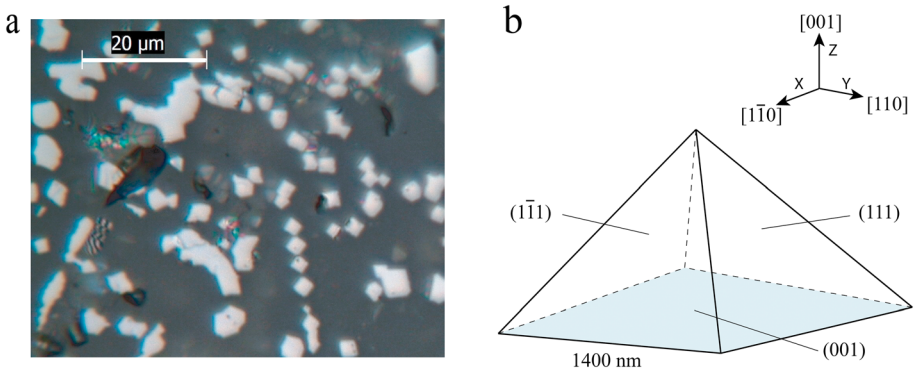


**Figure 1.** (a) Optical microscope image of a representative region of the TM54 sample. The magnetic grains (bright grains) are dispersed in non-magnetic silicate matrix. (b) Geometry of the micromagnetic model used in this study with corresponding crystallographic axes. MFM images were simulated for the base of the pyramid, which is a (001) plane (colored in gray).

average x = 0.54 (see supporting information), consistent with the composition determined by Curie temperature measurements. EBSD images were obtained from six titanomagnetite grains previously imaged with the MFM to examine the relationship between crystallographic orientation and magnetic microstructures. Probe conditions included an accelerating voltage of 20 kV with a working distance of 25 mm. Diffraction patterns were automatically collected for several spots per gain. Orientation data were processed using Matlab and Matlab toolbox MTex (mtex-toolbox.github.io; Hielscher & Schaeben, 2008).

### 2.3. Magnetic Force Microscopy

Magnetic domain observations were carried out using a magnetic force microscope (MFP-3D classic from Asylum Research). The MFM images were taken in noncontact AC mode at a constant scanning height of 50 nm with commercially available cantilevers and MFM tips. The standard magnetic tip with Co-Cr coating (tip radius = 35 nm) was magnetized in the *z* direction positive upward (perpendicular to the sample surface). The response of the MFM is then mostly sensitive to the second *z* derivative of the sample stray field ($d^2B_z/dz^2$) arising from magnetostatic charges produced by the divergence of the magnetization. To ensure that the magnetized tip did not affect the domain structures of the grains, some of the images were taken using different scan angles (Foss et al., 1998). The MFM images are the phase shift contrast in radians. MFM images were processed using Gwyddion software (Nečas & Klapetek, 2012).

MFM imaging was done on a subset of grains exhibiting shapes that were mostly quadrilateral varying from irregular trapezoids to nearly perfect squares. Grain size was determined by using the square root of surface area. Within this subset, grain size ranged from 1 to 4 μm with mean value and standard deviation of 1.6 ± 0.3 μm.

Domain structures were observed after alternating-field demagnetization (AFD) for 109 different titanomagnetite grains (see supporting information). AFD was achieved using an AC field with maximum peak field 200 mT applied in three perpendicular directions in the following order: *X*, *Y*, and *Z* (*Z* was perpendicular to the plain of observation). To image LEM states in six grains, we AF demagnetized the sample, took an MFM image, and then gave the sample a saturation remanent magnetization (SIRM), followed by another MFM image. We repeated this cycle 10 times and obtained 10 MFM images of AFD state and 10 MFM images of SIRM state. SIRM was imparted in the field of 1 T in the *Z* direction. In addition, we imaged magnetic microstructures in grain G25 after imparting of 1-T SIRM parallel to the surface plane (the *X* direction).

### 2.4. Micromagnetic Simulations

Micromagnetic simulations were conducted using the Micromagnetic Earth Related Robust Interpreter Language Laboratory (MERRIL), an open-source 3-D micromagnetic package designed for rock magnetic applications (Ó Conbhuí et al., 2018) and visualized using Paraview (Ahrens et al. 2005). Little experimental data have been published on magnetic constants at room temperature for intermediate titanomagnetite (Kakol et al., 1991; Sahu & Moskowitz, 1995; Syono, 1965), and there are no data for the exact composition

of TM54 studied here. Thus, the magnetic constants used in modeling were estimated/interpolated from existing data. Exchange constant, $A = 0.76 \times 10^{-11}$ J/m, was estimated from the dependence of Curie temperature on composition in titanomagnetite series (Butler & Banerjee, 1975). Saturation magnetization, $M_s = 156$ kA/m, and magnetocrystalline anisotropy, $K_1 = -1.0$ kJ/m$^3$, were obtained through linear interpolation from the dependence of $M_s$ and $K_1$ on composition, respectively (Hunt et al., 1995; Kakol et al., 1991). A negative $K_1$ makes the [111] direction a magnetocrystalline easy axis of magnetization identical to magnetite. Magnetostrictive and magnetoelastic effects are not incorporated in the current version of MERRILL. Whereas magnetostriction may need to be considered in modeling Ti-rich titanomagnetites, the resulting micromagnetic models appear to fit our observations without the inclusion of magnetostriction.

Geometry of the model was a square pyramid with four equilateral triangular faces (i.e., half-octahedron; Figure 1b). The triangular faces are {111} planes while the square face of the pyramid is a (001) plane. The edges of the base square are parallel to <110> directions. This particle geometry was chosen as more realistic for individual grains on a polished surface than simple cubic shapes and further justified by the EBSD data. The edge length of the base square was 1.4 μm. The mesh element size was 38 nm, which is larger than the exchange length, $L_{exch}$, of 22 nm for material with the magnetic constants used in the model ($L_{exch} = \sqrt{2A/\mu_0 M_s^2}$; e.g., Rave et al., 1998). Several models run with a finer mesh size of 22 nm did not noticeable change the solutions.

To find possible LEM states we ran 50 models starting from two different initial states: (1) a randomized initial state to simulate the AFD state and (2) an initial uniform state with magnetic moments parallel to [001] (e.g., *Z* direction) to simulate the SIRM state. The MFM response was calculated from the micromagnetic solutions for $M_x$, $M_y$, and $M_z$. We used a vertical point dipole approximation with constant magnetization for the MFM tip magnetization and calculated the second derivative of the *z* component of the stray field ($\partial^2 H_z/\partial z^2$) at 50 nm above the surface. Second derivatives of stray field were calculated only for the square base face of the pyramid which is (001) plane (Figure 1b). Therefore, our MFM simulations are maps of the variation of $\partial^2 H_z/\partial z^2$ at a fixed height (*z*) over the sample surface. Further details are provided in the supporting information.

## 3. Results

### 3.1. MFM Observations

To explore common ground domain states of small titanomagnetite grains, we imaged micromagnetic structures of 109 equidimensional TM54 grains (size 1–4 μm) after AFD. Our observations showed that magnetization in these particles tends to align parallel to the surface as indicated by the nearly constant MFM contrast over the surface of the grain. Nearly 80% of the grains displayed in-plane magnetization (Figures 2a–2e), while the remaining grains exhibited strong out-of-plane components (Figures 2g and 2h) or a combination of both in-plane and out-of-plane components of magnetization (Figure 2f).

We interpreted magnetic structures on 67 grains with in-plane magnetization. Of these, 15 grains contained no noticeable walls and appeared to be in the single domain or flower state (Figures 2a and 2b), 20 grains displayed two-domain states (Figures 2c and 2d), 21 grains exhibited three-domains states (Figure 2e), and 11 grains exhibited four-domain states (Figure 2f).

Remarkably, 85% of three- and four-domain states were formed by flux-closure or vortex-like structures (Figures 2e–2f). Most common were *X* and *Y* states shown in Figures 2e and 2f, respectively. We defined the *X* state as a vortex-like state with four nearly equal domains separated by 90° walls, and the *Y* state as a vortex-like state with one closure-like domain on one side of the grain bounded by two 90° walls (see schematic drawings in Figures 2e and 2f).

Although quantitative analysis of the MFM response profiles across walls are complicated and nonunique, simple profile symmetry arguments can be used to obtain qualitative information about the DW type (Foss et al., 1996, 1998). For example, with the MFM tip magnetized in the *z* direction, the MFM response profile ($\partial^2 H_z/\partial z^2$) of a pure Bloch wall (~vertical dipole with magnetization rotation within wall plane) would be symmetric about the midpoint of the wall, while a pure Néel wall (~horizontal dipole with magnetization rotation perpendicular to wall plane) would be antisymmetric. Hybrid walls consisting of both wall components produce asymmetric responses (Foss et al., 1996, 1998; Xu & Dunlop, 1996). Using this

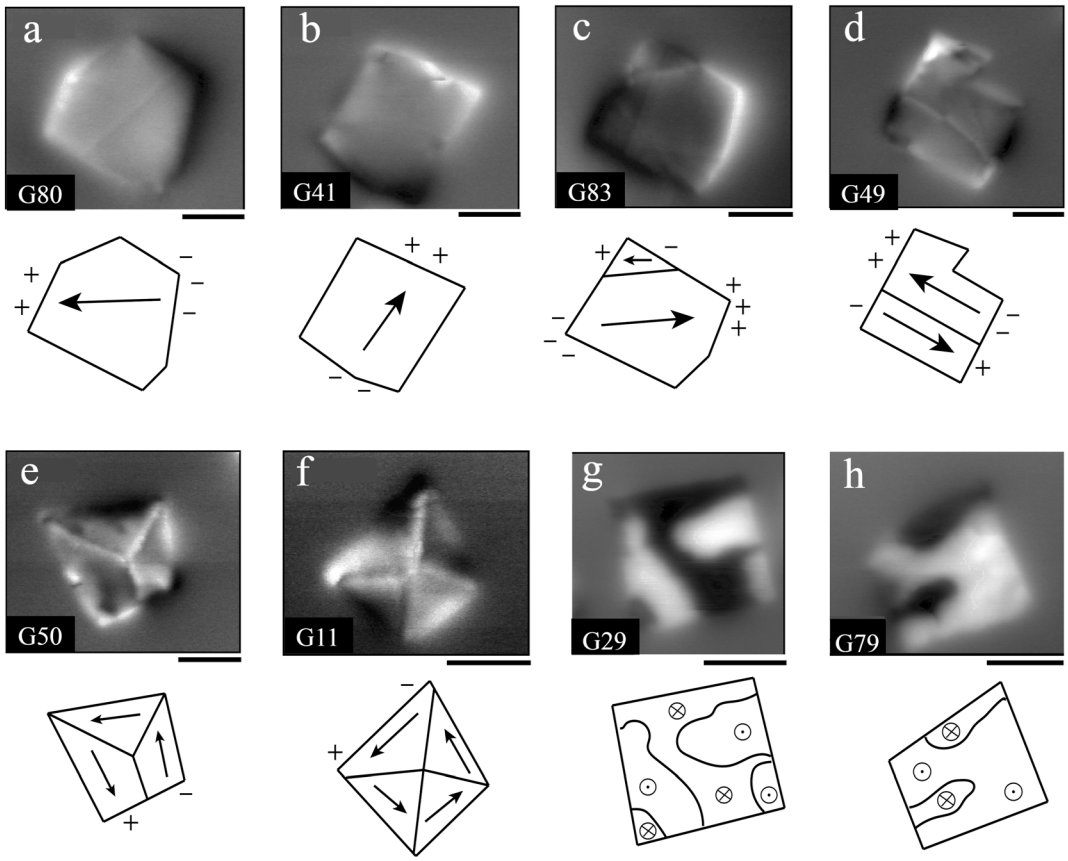


**Figure 2.** Examples of MFM images for domain states observed in 1–4-μm titanomagnetite grains. (a and b) Single-domain state. (c and d) Two-domain state. Flux-closure structures exhibiting (e) *Y* states and (f) *X* states. (g and h) Magnetic states with out-of-plane magnetization. MFM-image contrast represents the direction of magnetization in the sample. Dark (light) contrast corresponds to repulsive (attractive) interaction of the MFM tip with the sample stray field. (a)–(f) display mainly in-plane magnetization with contrast only in transition regions (e.g., domain walls) and on the grain edges. When magnetization is perpendicular to the surface like in (g) and (h), black (magnetization points out) and white (magnetization points in) regions are observed. Gray areas or no contrast appear when magnetization of the sample is approximately parallel to the surface. The arrows in the schematic drawings indicate the magnetization direction within magnetic domains. "Plus sign" and "minus sign" indicate magnetic poles on the grain edges. Scale bars are 1 μm.

symmetry argument, magnetic domains with *X* and *Y* configurations were separated by transitional regions which resemble 90° and 180° Néel-like domain walls. In such walls, magnetization rotates in-plane creating antisymmetric MFM-response profiles. This type of wall usually forms in thin films to reduce magnetostatic energy at the surface (e.g., Hubert & Schäfer, 1998), although it has also been observed in edge-spike domains in micron-sized particles of magnetite (Pokhil & Moskowitz, 1997). The thickness of these transitional regions in TM54 was determined from 2-D wall profiles as the distance between minimum and maximum of the profile curve (see Figure 8). For 26 grains, the wall width ranged between 110 and 182 nm with the mean value and standard deviation of 145 ± 21 nm.

**Table 1**
*Crystallographic Orientations in Six Grains*

| Grain no. | Size[a] (μm) | Angle between surface and (001) | Angle between surface plane and {111} crystallographic directions | | | |
|---|---|---|---|---|---|---|
| | | | [111] | $[11\bar{1}]$ | $[1\bar{1}1]$ | $[\bar{1}11]$ |
| G2 | 1.5 | 15° | 46° | −24° | 26° | 44° |
| G11 | 1.4 | 11° | 45° | −25° | 39° | 30° |
| G25 | 1.5 | 13° | 45° | −25° | 43° | 27° |
| G49 | 1.9 | 24° | 57° | −12° | 39° | 25° |
| G50 | 1.6 | 41° | 57° | −2° | 52° | 5° |
| G56 | 3.8 | 10° | 45° | −26° | 36° | 33° |

[a]Square root from surface area.

### 3.2. Crystallographic Orientations

To facilitate the MFM interpretation, we determined crystallographic orientations in six grains (G2, G11, G25, G49, G50, G56) after MFM imaging (Table 1). Four square-shaped grains that exhibited similar (vortex-like) magnetic structures (G2, G11, G25, and G56) had similar surface orientations. In these grains, the surface planes made small angles (10°–15°) with a (001) plane (Figures 3a and 3c), while the nearest <111> directions intersected the surface at larger angles (25°–45°). The

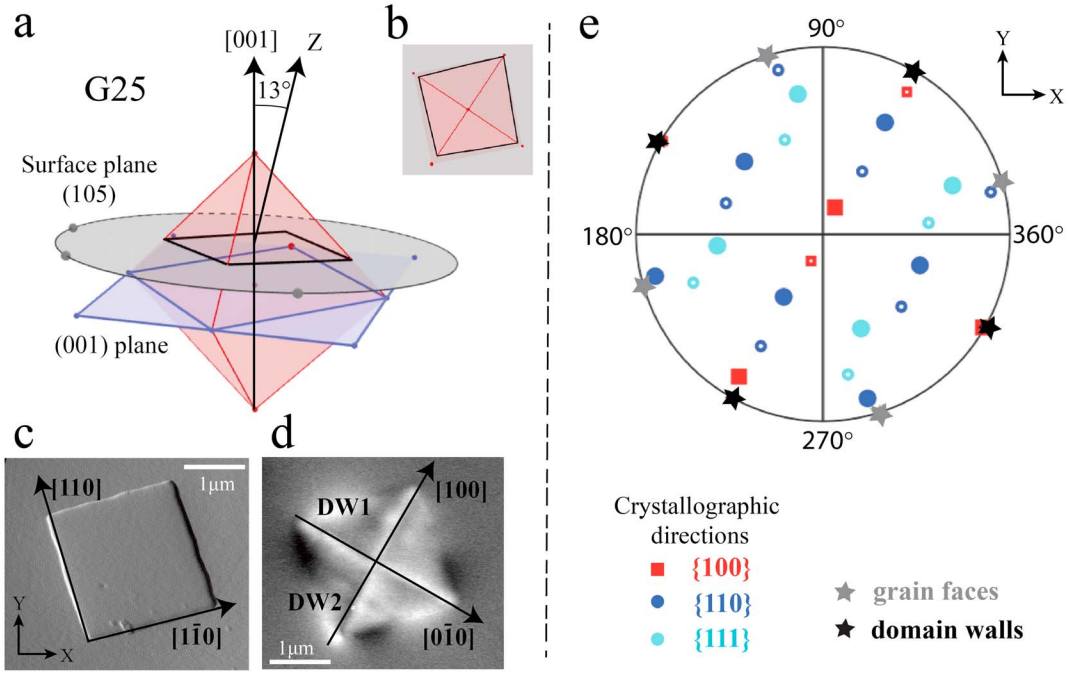


**Figure 3.** Orientation of the surface in grain G25. (a) The 3-D representation of (105) cutting plane of octahedral crystal (*Z* is direction perpendicular to the surface plane). (b) Theoretical shape of the grain (view from above). (c) Topographical image of the grain with projections of the [110] and $[1\bar{1}0]$ directions on the surface plane. Inclination of [110] and $[1\bar{1}0]$ were 10° and 8°, respectively. (d) MFM image of the grain with projections of the $[0\bar{1}0]$ and [100] directions on the surface plane. (e) Pole figure of crystallographic directions in the sample's coordinate system and declinations of the grain faces and domain walls. Filled (open) symbols correspond to directions with positive (negative) inclination. The declinations of the grain faces and domain walls were measured as angle between the *X* direction in sample coordinate system and the line of a grain face or domain wall in counterclockwise direction.

edge faces of the grains were 0°–5° from the projections of <110> crystallographic directions on the surface plane. Domain walls were subparallel (<5°) to the surface projections of <100> directions (Figure 3d), and the MFM contrasts within the domains were nearly uniform indicating mainly in-plane magnetizations. Using the EBSD data and the almost perfect square shape of these grains, we infer that their 3-D shapes are approximately a square pyramid.

Two grains that had irregular quadrilateral shapes (G49, G50) and different magnetic structures displayed surface planes at significantly larger angles to a (001) plane. Grain G49 with a two-domain state had its surface plane inclined 24° from (001), making one of the <111> directions nearly parallel to the surface (inclination 12°). Grain G50 with a three-domain state had its surface inclined 41° from the (001) plane making two <111> axes nearly parallel to the surface (inclinations <5°).

### 3.3. LEM States in Six Grains

To explore possible local energy minimum (LEM) states, we imaged 10 states after AFD and 10 states after SIRM (field applied perpendicular to the surface) on six grains with known crystallographic orientations from EBSD data. Our observations showed that four grains that had similar surface orientations displayed common LEM states (Figure 4), whereas grains G49 and G50 with different surface orientations displayed additional types of LEM states (Figure 5).

*X* state and *Y* state were the two most common LEM states for grains G2, G11, and G25 with similar surface orientations and ~1.5-μm size. Figures 4a1 and a2, 4b1 and b2, and 4c1 and c2 show pairs of *X* states observed in these grains. Note that magnetization rotates counterclockwise in images a1, b1, and c1, and clockwise in images a2, b2, and c2, which corresponds to two chirality states of the magnetic vortex. Figures 4a4, 4b3–b5, and 4c5–c8 show *Y* states observed in grain G2, G11, and G25. In grain G25, we observed three distinct *Y* states symmetrical about a center point (Figure 4c5, c7, and c8). Similar to *X* states, the *Y* state occurred with either clockwise or counterclockwise vortex rotations (Figure 4c5 and c6, respectively).

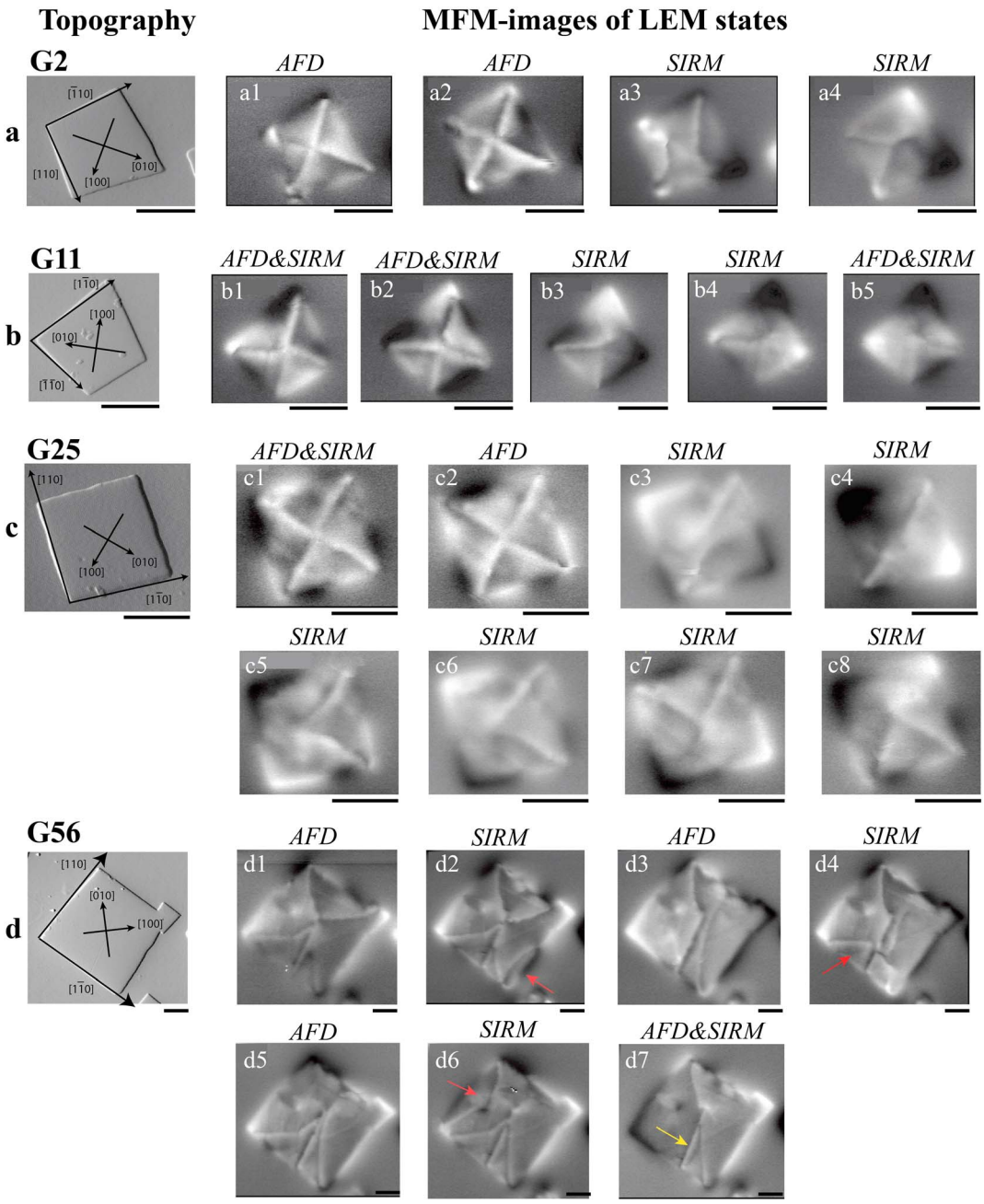


**Figure 4.** LEM states in four different grains of TM54 with similar surface orientations which are inclined 10°–15° to (001) crystallographic plane. Images on the left show grain topography with projections of crystallographic {110} directions on the surface plane. Initial magnetic states (AFD, SIRM) that produced LEM states are shown on top of MFM-images. AFD&SIRM indicates that particular LEM state was observed after both types of experiments. a1–a2, b1–b2, and c1–c2 are pairs of *X* states with opposite chirality: counterclockwise and clockwise rotation of magnetization, respectively; a3 and c3 are double-vortex states; a4, b3–b5, and c5–c8 are *Y* states; d1, d3, and d5 are *X* state, double vortex, and *Y* state observed in grain G56 after AFD; and d2, d4, and d6 are *X* state, double vortex, and *Y* state observed in grain G56 after SIRM. Red arrows indicate small domains emerging on the grain edges, and yellow arrow indicates a surface scratch. d7 is a two-domain state in grain G56. Scale bars are 1 μm.

The *X* state was the dominant LEM state after AFD, whereas *Y* state was the dominant state after SIRM in the *Z* direction. For example, G25 displayed nine *X* states (six with counterclockwise rotation and three with clockwise rotation) and one *Y* state after AFD. In contrast, it exhibited only one *X* state but eight *Y* states after SIRM.

In addition to *X* and *Y* states, grains G2 and G25 displayed a third type of LEM states that occurred after imparting an SIRM in *X* direction (Figures 4a3 and 4c3). These configurations had two domain walls

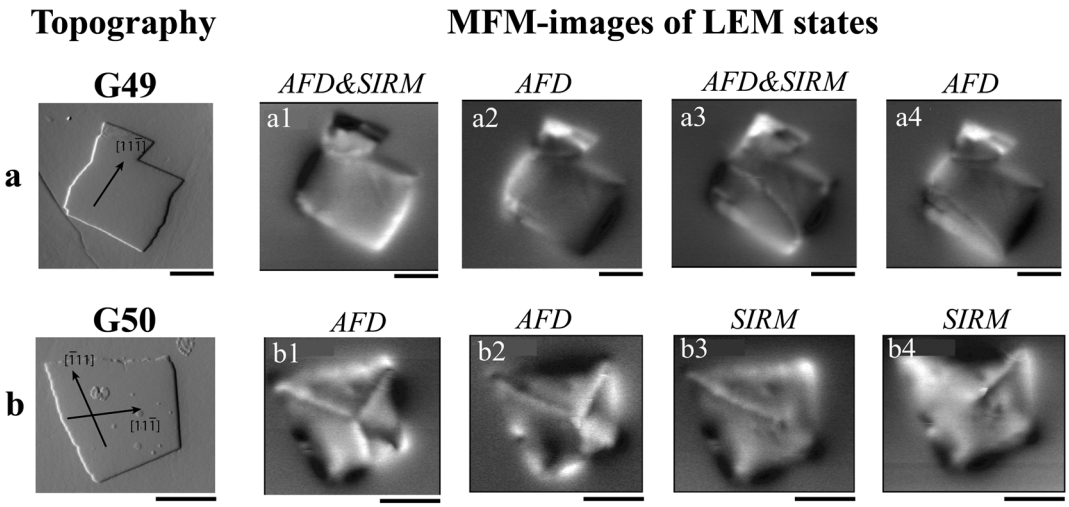


**Figure 5.** LEM states in grains G49 and G50 of TM54. Surface orientations are 24° and 41° to (001) crystallographic plane, respectively. Images on the left show grain topography with projections of {111} directions nearest to the surface plane. Initial magnetic states (AFD, SIRM) that produced LEM states are shown on top of MFM-images. AFD&SIRM indicates that particular LEM state was observed after both types of experiments. Scale bars are 1 μm.

reminiscent of a traditional three-domain state or possibly a double-vortex (DV) state. G25 also displayed a fourth type of LEM state after SIRM in plane (the *X* direction) shown in Figure 4c4.

Analogous *X*, *Y*, and DV LEM states were observed after AFD in grain G56 (Figure 4d1, d3, and d5). This grain had a similar surface orientation as grains G2, G11, and G25, but was larger in size (~3.5 μm). However, G56 exhibited a greater variety of LEM states after imparting SIRM. The basic domain configuration remained the same (*X*, *Y*, or DV state), but smaller domains occurred on the sides of the grain (Figure 4d2, d4, and d6). These smaller domains resembled conventional domains in multidomain grains. Also, in grain G56, the two-domain state occurred 7 out of 10 times after AFD (Figure 4d7). This two-domain state is more likely to be a ground state for grain G56, in contrast to an *X* state for smaller-sized grains discussed above. Note that grain G56 has a long deep scratch on its surface which originates near the center of the grain and propagates perpendicularly to the edge of the grain (see Figure 4d7). Such surface defect may affect the domain configuration on the surface, that is, acting as a pinning or nucleation site for domain walls.

Grain G49 had two basic LEM states: a single-domain like state and a two-domain configuration (Figure 5a). The most frequent configuration for both AFD and SIRM states was the single-domain like state (Figure 5a1 and a2). Considering the fact that this grain had a <111> direction subparallel to surface plane (~12°), it is possible that it is a single-vortex state with the vortex core aligned in-plane along <111> easy axis (assuming $K_1 < 0$).

LEM states observed in grain G50 are shown in Figure 5b. All AFD states were represented by *Y* states with different vortex rotations: four clockwise and six counterclockwise (Figure 5b1 and b2, respectively). The LEM state shown in Figure 5b3 occurred 9 times, and the state shown in Figure 5b4 occurred once after imparting SIRM. Both states displayed a domain wall which starts at one corner and disappears toward the center of the grain.

### 3.4. Micromagnetic Modeling

Fifty micromagnetic simulations of a 1.4-μm pyramid grain of TM54 revealed four discrete LEM states. The single-vortex (SV) state shown in Figure 6a occurred 35 times (70%) and had the lowest total energy of $\sim 1.4 \times 10^{-16}$ J. The simulated MFM image of the SV model is similar to the observed *X* state in our titanomagnetite grains (Figure 7a). It displays four flux-closure domains separated by 90° Néel-like domain walls.

The double-vortex (DV) state shown in Figure 6b occurred 8 times (16%) and had a higher total energy of $\sim 1.8 \times 10^{-16}$ J. The simulated MFM image of the DV model is similar to the observed two-domain like structures (Figure 7b). It displays two Néel-like domain walls that originate at the opposite corners of the grain and disappear within the grain and failing to reach the opposite edge of the grain.

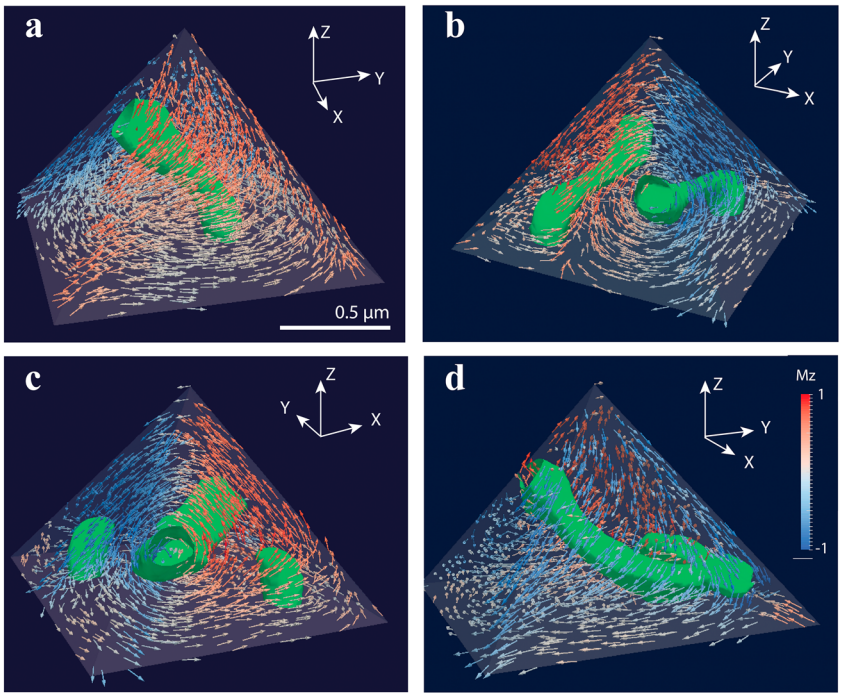


**Figure 6.** (a–d) LEM states in 1.4-μm pyramid grain of TM54 starting from an initial randomized magnetization. Arrows represent magnetization direction and are color coded by the vertical component of the magnetization vector ($M_z$). Blue/red color corresponds to down/up direction. The vortex cores are indicated by green contours defined by helicity of the magnetization ($\vec{M}\cdot\left(\vec{\nabla}\times\vec{M}\right)$).

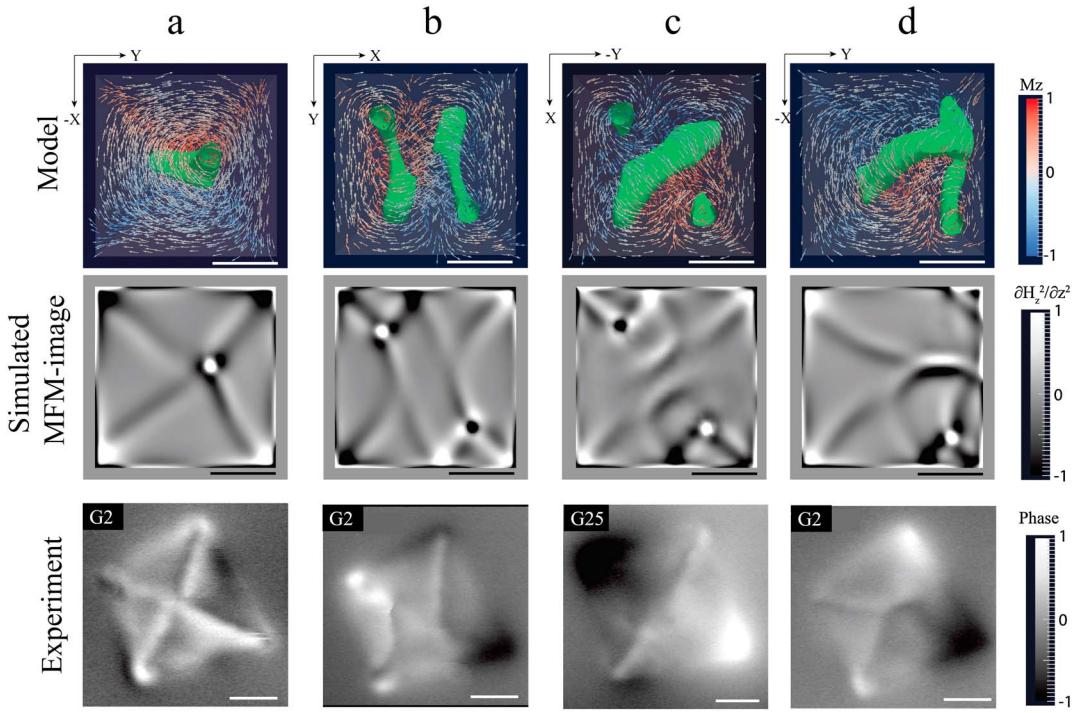


**Figure 7.** (a–d) Comparison of computer simulations and observed LEM states in ~1.5-μm TM54 grains. (top) Model results viewed on a square face of pyramid, (middle) MFM images simulated on the square face of pyramid, and (bottom) examples of MFM images of similar LEM states observed in grains G2 and G25. Scale bars are 0.5 μm.

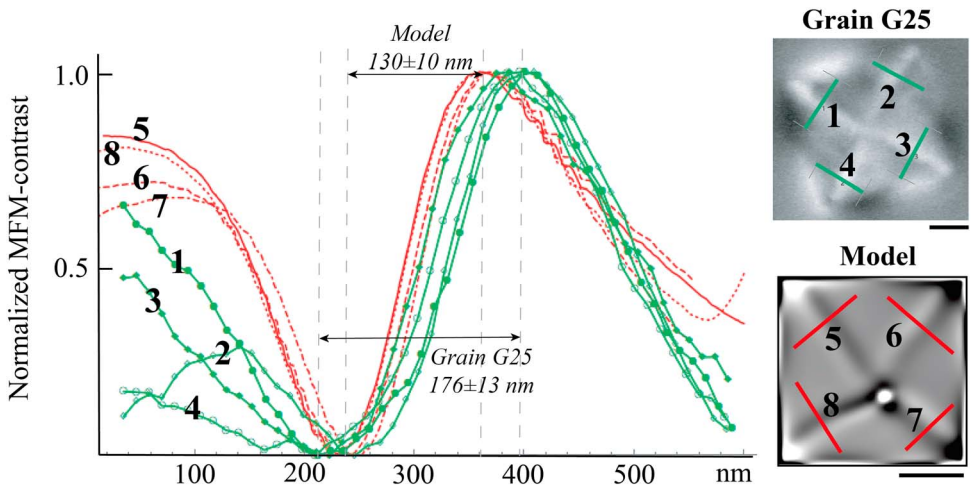


**Figure 8.** (left) Comparison of two-dimensional domain wall profiles from vortex state in grain G25 and from simulated single-vortex state. (right, top) MFM image of G25 and (bottom) simulated MFM image from the model. Profile numbers correspond to the line numbers on MFM images of grain G25 (green) and the model (red). Each observed profile (1–4) represents an average of 30 individual line profiles. The vertical axis is a normalized MFM contrast ($\partial 2$ Hz/$\partial z2$) in range from 0 to 1 (minimum values of the profiles set to 0 and maximum values of the profiles set to 1). Scale bars are 0.5 μm.

The third LEM state occurred 5 times (10%) with a total energy of ~$2.1 \times 10^{-16}$ J (Figure 6c). This multivortex state contained one large and two small vortex cores. Grain G25 exhibited similar state after imparting SIRM in plane (the *X* direction; Figure 7c).

The fourth LEM state (Figure 6d) had the largest total energy of ~$2.3 \times 10^{-16}$ J of the four states and occurred only twice (4%). It consisted of a main vortex core that branched out into two smaller vortex cores near a corner of the particle. Similar multivortex LEM state resulted from the micromagnetic simulation starting from an initial uniform state magnetization in the *Z* direction which corresponds to the SIRM state in the experiment. The simulated MFM image from this model resembled the *Y* states observed in the titanomagnetite grains after imparting SIRM (Figure 7d).

Domain wall profiles from the simulated MFM image of a single-vortex and the observed *X* states agree qualitatively and display similar antisymmetric shapes with a slight asymmetric component (Figure 8). We estimated the domain wall thickness in these Néel-like walls as the distance between the maximum and minimum points in the profiles as shown in Figure 8. For example, the average domain wall thickness observed in grain G25 was 176 ± 13 nm, which is slightly wider than in the model (130 ± 10 nm). Other than uncertainty in material constants in the model, a broader MFM response in the experiment is expected due to the influence of the local magnetic field of the MFM tip on domain walls, as well as the integrated effect over the tip itself (rather than assuming just a point dipole), both of which were not taken into account in the simulated MFM image (e.g., Foss et al., 1996).

## 4. Discussion

This is the first study that reports clear evidence for vortex states in intermediate titanomagnetite. Interestingly, Geiß et al. (1996) reported Bitter patterns from small inclusions (~1–2 μm) of oxidized titanomagnetite (~TM60) in volcanic ash particles. For some grains and applied field conditions observed near the limits of optical resolution, the Bitter patterns consisted of just sparse patches of colloid accumulations, which they speculated might be the result of a vortex state. However, the patches transform into more domain-like features when the field was changed suggesting possible wall nucleation sites instead.

Domain structures with planar or wavy domain patterns were reported previously on intermediate titanomagnetite (e.g., Ambatiello & Soffel, 1996; Halgedahl & Fuller, 1980, 1983; Moskowitz et al., 1988; Soffel et al., 1990). These studies focused on larger titanomagnetite grains (>10 μm) and attributed observed domain structures to a uniaxial anisotropy controlled by stress. However, the majority of flux-closure structures observed in our study suggest that for smaller grain sizes, other types of

anisotropy might be dominant such as shape anisotropy or magnetocrystalline anisotropy. This is supported by the observation of the dependence of micromagnetic structures and LEM states on the crystallographic orientation of the surface of the grain. Furthermore, the micromagnetic models did not incorporate any stress-dependent properties, but still were able to duplicate the main features observed with MFM. There have been relatively few attempts to incorporate magnetoelastic effects into micromagnetic models (Fabian & Heider, 1996; Liang et al., 2014), but recent results for TM60 (Ó Conbhuí, 2017) suggest that the evolution of domain structure is not greatly affected by magnetostriction but that the critical grain sizes may change by a percent dependent on grain shape. The good match between the numerical models and MFM observations that we show here would support this finding, at least when the main LEM state is a vortex state. Nevertheless, domain structures like those observed for grains G29 and G79 (Figures 2g and 2h) that exhibit an out-of-plane magnetization and stripe-like domain patterns suggest a uniaxial anisotropy that is likely of stress origin. The crystallographic orientations of these two grains are not known, but none of our micromagnetic models reproduced these particular states.

Our observations of nonuniform micromagnetic structures in 1–4-μm grains of TM54 are in broad agreement with previous theoretical calculations (Butler & Banerjee, 1975; Rave et al., 1998) and approximations from experimental data (Soffel, 1977) that predicted nonuniform magnetization in grains of TM54 above ~165 nm. Also, in a larger grain size (G56, ~3.5 μm), we observed vortex states combined with more classical domains characteristic of multidomain states. This finding agrees well with micromagnetic calculations (Rave et al., 1998) that predicted PSD to MD transition at 3-μm grain size for materials with magnetic constants similar to TM54.

We imaged four reproducible discrete LEM states in ~1.5-μm grains with similar surface orientations. Our observations are remarkably consistent with our 3-D micromagnetic model and simulated MFM images of ~1.4-μm pyramid grain of TM54. A single vortex (*X* state) was the most frequent state observed after AFD (Figures 4a1 and a2, 4b1 and b2, and 4c1 and c2). Likewise, the micromagnetic model showed a single-vortex state as the most frequent state which corresponded to the lowest total energy (Figure 6a). The simulated MFM image from single vortex is similar to the observed *X* states (Figure 7a).

The *Y* state (Figures 4a5, 4b3–b5, and 4c4–c8) was the most common state observed after SIRM in the *Z* direction. The model exhibited a multivortex LEM state after initial uniform magnetization in the *Z* direction that produced MFM images very similar to the observed *Y* state (Figure 7d). This *Y* state was in fact the highest-energy LEM state in our model. These findings suggest that a single-vortex state is most likely a ground state, whereas the multivortex (*Y* state) is a higher-energy state for the given grain size and shape of TM54.

In addition, both observation and model revealed existence of double-vortex LEM states, which according to the model had a slightly higher energy than the single-vortex state (Figures 4c3 and 6b) and another multivortex state (Figures 4c4 and 6c). If the model is correct and a double vortex indeed has just slightly higher energy than single vortex, we would expect to see double-vortex states more frequently than the *Y* state after AFD. However, we did not observe any double-vortex states after AFD and just a few *Y* states. The reason for that might lie in the insufficient number of experiments to provide a good statistical sampling of LEM space or in the experimental setup itself. To achieve AFD in three dimensions we demagnetized the sample sequentially in three perpendicular directions *X*, *Y*, and then *Z* (sample coordinates), where the *Z* direction was perpendicular to the sample surface. It is possible that the last direction of demagnetization (*Z*) determines the most probable states that would occur after AFD (in our case that would be the *X* state as a ground state and *Y* state as a SIRM state). To test this possibility, additional experiments with AFD performed in different cyclical order are required and will be addressed in another study.

Based on the agreement between our observations and micromagnetic modeling, we interpret that most of the investigated grains have a single vortex as a ground state. The variation in domain structures we observed from single domain to four domains might then result from the different cutting planes of octahedral crystals and the resulting 3-D shape of the grains. Recent findings about extremely stable vortex states in magnetite (Almeida et al., 2014, 2016; Nagy et al., 2017) combined with our observations of vortex states in titanomagnetite grains (1–5 μm) suggest that vortex states are probably a common micromagnetic state occurring at the lower end of the PSD size range (Roberts et al., 2017). For natural titanomagnetite (x~0.5), this size range is known to carry stable and reliable remanence.

## 5. Conclusions

Our MFM results show that TM54 grains with mainly in-plane magnetization contain one to four domains, vortex-like or flux-closure structures, and Néel-like walls. These findings suggest that the magnetostatic energy (shape anisotropy) outweighs the magnetocrystalline anisotropy energy for this grain size.

Average domain wall thickness estimated from MFM images of 26 grains was 145 ± 21 nm and is consistent with the micromagnetic model that exhibited slightly narrower domain walls (130 ± 10 nm).

We found that domain structure depends on the crystallographic orientation of grain surfaces and thereby on grain shape, similar to the MFM results found for magnetite by Pokhil and Moskowitz (1996). For randomly oriented grains, crystallographic data from electron backscatter diffraction and numerical micromagnetic modeling are critical for MFM interpretation.

*X* states and three types of multivortex states were the four discrete LEM states observed in ~1.5-μm grains. Vortex states with *X* domain configuration is most likely the lowest-energy state (ground state) for this grain size and shape, whereas multivortex domain configurations are higher-energy states.

Our micromagnetic model of ~1.5-μm square pyramid agrees well with the experimental results showing single vortex as a ground state and multivortices states as higher-energy states.

Larger grain (~3.5 μm) displayed transitional LEM states which combined either *X*, *Y*, or double vortex with classical domains characteristic to multidomain grains.

About 20% of the grains imaged exhibited out-of-plane magnetization and stripe-like domain patterns suggesting a uniaxial anisotropy that is likely of stress origin. None of our micromagnetic models reproduced these states.

**Acknowledgments**
We thank Adrian Muxworthy and Joshua Einsle for the thoughtful reviews. This research was supported by National Science Foundation (NSF) grant EAR1446998. Parts of this work was carried out in the Characterization Facility, University of Minnesota, which receives partial support from NSF through the MRSEC program. The Institute for Rock Magnetism is supported by grants from the Instruments and Facilities Program, Division of Earth Science, NSF. The numerical modeling was carried out with support from the Natural Environment Research Council (grant NE/J020966/1) and the European Research Council (grant EC320832). A.R. Biedermann was supported by the Swiss National Science Foundation, project 167608. The data used in this paper are included in the supporting information. This is IRM contribution 1809.

## References

Ahrens, J., Geveci, B., & Law, C. (2005). ParaView: An end-user tool for large data visualization. In C. D. Hansen & C. R. Johnson (Eds.), *The Visualization Handbook* (pp. 717–732). Elsevier. Retrieved from www.paraview.org

Almeida, T. P., Kasama, T., Muxworthy, A. R., Williams, W., Rafal, E., Kensington, S., & Road, W. M. (2014). Observing thermomagnetic stability of magnetite particles: Good paleomagnetic recorders? *Geophysical Research Letters*, *41*, 7041–7047. https://doi.org/10.1002/2014GL061432

Almeida, T. P., Muxworthy, A. R., Kovács, A., Williams, W., Nagy, L., Conbhuí, P., et al. (2016). Direct observation of the thermal demagnetization of magnetic vortex structures in nonideal magnetite recorders. *Geophysical Research Letters*, *43*, 8426–8434. https://doi.org/10.1002/2016GL070074

Ambatiello, A., & Soffel, H. C. (1996). Kerr microscopy of small synthetic Ti-rich titanomagnetite grains. *Geophysical Research Letters*, *23*(20), 2807–2810. https://doi.org/10.1029/96GL00447

Appel, E. (1987). Stress anisotropy in Ti-rich titanomagnetites. *Physics of the Earth and Planetary Interiors*, *46*(1–3), 233–240. https://doi.org/10.1016/0031-9201(87)90185-3

Appel, E., & Soffel, H. C. (1984). Model for the domain state of Ti-rich titanomagnetites. *Geophysical Research Letters*, *11*(3), 189–192. https://doi.org/10.1029/GL011i003p00189

Butler, R. F., & Banerjee, S. K. (1975). Theoretical single-domain grain size range in magnetite and titanomagnetite. *Journal of Geophysical Research*, *80*(29), 4049–4058. https://doi.org/10.1029/JB080i029p04049

Dahlberg, E. D., & Zhu, J. (1995). Micromagnetic microscopy and modeling. *Physics Today*, *48*(4), 34–40. https://doi.org/10.1063/1.881447

De Groot, L. V., Fabian, K., Bakelaar, I. A., & Dekkers, M. J. (2014). Magnetic force microscopy reveals meta-stable magnetic domain states that prevent reliable absolute palaeointensity experiments. *Nature Communications*, *5*(1), 1–10. https://doi.org/10.1038/ncomms5548

Dunlop, D. J., & Özdemir, Ö. (1997). *Rock Magnetism: Fundamentals and Frontiers*. New York: Cambridge University Press. https://doi.org/10.1017/CBO9780511612794

Fabian, K. (2006). Approach to saturation analysis of hysteresis measurements in rock magnetism and evidence for stress dominated magnetic anisotropy in young mid-ocean ridge basalt. *Physics of the Earth and Planetary Interiors*, *154*(3-4), 299–307. https://doi.org/10.1016/j.pepi.2005.06.016

Fabian, K. (2012). Comment on "Detecting uniaxial single domain grains with a modified IRM technique" by R. Mitra, L. Tauxe and J. S. Gee. *Geophysical Journal International*, *191*(1), 42–45. https://doi.org/10.1111/j.1365-246X.2012.05478.x

Fabian, K., & Heider, F. (1996). How to include magnetostriction in micromagnetic models of titanomagnetite grains. *Geophysical Research Letters*, *191*(1), 42–45. https://doi.org/10.1111/j.1365-246X.2012.05478.x

Fabian, K., & Hubert, A. (1999). Shape-induced pseudo-single-domain remanence. *Geophysical Journal International*, *138*(3), 717–726. https://doi.org/10.1046/j.1365-246X.1999.00916.x

Feinberg, J. M., Scott, G. R., Renne, P. R., & Wenk, H. R. (2005). Exsolved magnetite inclusions in silicates: Features determining their remanence behavior. *Geology*, *33*(6), 513–516. https://doi.org/10.1130/G21290.1

Foss, S., Moskowitz, B. M., Proksch, R., & Dahlberg, E. D. (1998). Domain wall structures in single-crystal magnetite investigated by magnetic force microscopy. *Journal of Geophysical Research*, *103*(B12), 30,551–30,560. https://doi.org/10.1029/98JB00152

Foss, S., Proksch, R., Dahlberg, E. D., Moskowitz, B., & Walsh, B. (1996). Localized micromagnetic perturbation of domain walls in magnetite using a magnetic force microscope. *Applied Physics Letters*, *69*(22), 3426–3428. https://doi.org/10.1063/1.117281

Frandsen, C., Stipp, S. L. S., McEnroe, S. a., Madsen, M. B., & Knudsen, J. M. (2004). Magnetic domain structures and stray fields of individual elongated magnetite grains revealed by magnetic force microscopy (MFM). *Physics of the Earth and Planetary Interiors*, *141*(2), 121–129. https://doi.org/10.1016/j.pepi.2003.12.001

Gee, J., & Kent, D. V. (1995). Magnetic hysteresis in young mid-ocean ridge basalts: Dominant cubic anisotropy? *Geophysical Research Letters*, *22*(5), 551–554. https://doi.org/10.1029/95GL00263

Geiß, C. E., Heider, F., & Soffel, H. C. (1996). Magnetic domain observations on magnetite and titanornaghemite grains (0.5–10 μm). *Geophysical Journal International*, *124*(1), 75–88. https://doi.org/10.1111/j.1365-246X.1996.tb06353.x

Halgedahl, S., & Fuller, M. (1983). The dependence of magnetic domain structure upon magnetization state with emphasis upon nucleation as a mechanism for pseudo-single-domain behavior. *Journal of Geophysical Research*, *88*(B8), 6505. https://doi.org/10.1029/JB088iB08p06505

Halgedahl, S. L. (1987). Domain pattern observations in rock magnetism: Progress and problems. *Physics of the Earth and Planetary Interiors*, *46*(1-3), 127–163. https://doi.org/10.1016/0031-9201(87)90178-6

Halgedahl, S. L., & Fuller, M. (1980). Magnetic domain observations of nucleation processes in fine particles of intermediate titanomagnetite. *Nature*, *288*(5786), 70–72. https://doi.org/10.1038/288070a0

Hielscher, R., & Schaeben, H. (2008). A novel pole figure inversion method: Specification of the MTEX algorithm. *Journal of Applied Crystallography*, *41*(6), 1024–1037. https://doi.org/10.1107/S0021889808030112

Hodych, J. P., & Matzka, J. (2004). Saturation magnetostriction and its low temperature variation inferred for natural titanomaghemites: Implications for internal stress control of coercivity in oceanic basalts. *Geophysical Journal International*, *157*(3), 1017–1026. https://doi.org/10.1111/j.1365-246X.2004.02231.x

Hoffmann, V., Schafer, R., Appel, E., Hubert, A., & Soffel, H. (1987). First domain observations with the magneto-optical Kerr effect on Ti-ferrites in rocks and their synthetic equivalents. *Journal of Magnetism and Magnetic Materials*, *71*(1), 90–94. https://doi.org/10.1016/0304-8853(87)90336-2

Hubert, A., & Schäfer, R. (1998). *Magnetic Domains* (Vol. 40, p. 109). Berlin Heidelberg: Springer. https://doi.org/10.1049/sqj.1970.0020

Hunt, C. P., Moskowitz, B. M., & Banerjee, S. K. (1995). Magnetic properties of rocks and minerals. In T. J. Ahrens (Ed.), *Rock Physics and Phase Relations, A Handbook of Physical Constants* (Vol. 3, pp. 189–204) Washington, DC: American Geophysical Union.

Jackson, M., & Solheid, P. (2010). On the quantitative analysis and evaluation of magnetic hysteresis data. *Geochemistry, Geophysics, Geosystems*, *11*, Q04Z15. https://doi.org/10.1029/2009GC002932

Kakol, Z., Sabol, J., & Honig, J. M. (1991). Magnetic anisotropy of titanomagnetites, $Fe_{3-x}Ti_xO_4$, $0<x<0.55$. *Physical Review B*, *44*(5), 2198–2204. https://doi.org/10.1103/PhysRevB.44.2198

Kimura, Y., Sato, T., Nakamura, N., Nozawa, J., Nakamura, T., Tsukamoto, K., & Yamamoto, K. (2013). Vortex magnetic structure in framboidal magnetite reveals existence of water droplets in an ancient asteroid. *Nature Communications*, *4*(1), 1–8. https://doi.org/10.1038/ncomms3649

Krása, D., Shcherbakov, V. P., Kunzmann, T., & Petersen, N. (2005). Self-reversal of remanent magnetization in basalts due to partially oxidized titanomagnetites. *Geophysical Journal International*, *162*(1), 115–136. https://doi.org/10.1111/j.1365-246X.2005.02656.x

Lattard, D., Engelmann, R., Kontny, A., & Sauerzapf, U. (2006). Curie temperatures of synthetic titanomagnetites in the Fe-Ti-O system: Effects of composition, crystal chemistry, and thermomagnetic methods. *Journal of Geophysical Research*, *111*, B12S28. https://doi.org/10.1029/2006JB004591

Liang, C.-Y., Keller, S. M., Sepulveda, A. E., Bur, A., Sun, W.-Y., Wetzlar, K., & Carman, G. P. (2014). Modeling of magnetoelastic nanostructures with a fully coupled mechanical-micromagnetic model. *Nanotechnology*, *25*(43). https://doi.org/10.1088/0957-4484/25/43/435701

Mitra, R., Tauxe, L., & Gee, J. S. (2011). Detecting uniaxial single domain grains with a modified IRM technique. *Geophysical Journal International*, *187*(3), 1250–1258. https://doi.org/10.1111/j.1365-246X.2011.05224.x

Moskowitz, B. M., Halgedahl, S. L., & Lawson, C. A. (1988). Magnetic domains on unpolished and polished surfaces of titanium-rich titanomagnetite. *Journal of Geophysical Research*, *93*(B4), 3372–3386. https://doi.org/10.1029/JB093iB04p03372

Muxworthy, A. R., & Williams, W. (2006). Observations of viscous magnetization in multidomain magnetite. *Journal of Geophysical Research*, *111*, B01103. https://doi.org/10.1029/2005JB003902

Nagy, L., Williams, W., Muxworthy, A. R., Fabian, K., Almeida, T. P., Ó Conbhui, P., & Shcherbakov, V. P. (2017). Stability of equidimensional pseudo—Single-domain magnetite over billion-year timescales. *PNAS*, *114*(39), 10,356–10,360. https://doi.org/10.1073/pnas.1708344114

Nečas, D., & Klapetek, P. (2012). Gwyddion: An open-source software for SPM data analysis. *Open Physics*, *10*(1). https://doi.org/10.2478/s11534-011-0096-2

Ó Conbhuí, P., (2017). Micromagnetic modelling of imperfect crystals, PhD Thesis, Edinburgh University.

Ó Conbhuí, P., Williams, W., Fabian, K., Phil, R., Lesleis, N., & Muxworthy, A. R. (2018). MERRILL: Micromagnetic earth related robust interpreted language laboratory. *Geochemistry, Geophysics, Geosystems*, *19*, 1080–1106. https://doi.org/10.1002/2017GC007279

Pan, Q., Pokhil, T. G., & Moskowitz, B. M. (2002). Domain structures in epitaxial (110) $Fe_3O_4$ particles studied by magnetic force microscopy. *Journal of Applied Physics*, *91*(9), 5945–5950. https://doi.org/10.1063/1.1467401

Pokhil, T. G., & Moskowitz, B. M. (1996). Magnetic force microscope study of domain wall structures in magnetite. *Journal of Applied Physics*, *79*(8), 6064. https://doi.org/10.1063/1.362093

Pokhil, T. G., & Moskowitz, B. M. (1997). Magnetic domains and domain walls in pseudo-single-domain magnetite studied with magnetic force microscopy. *Journal of Geophysical Research*, *102*(B10), 22,681–22,694. https://doi.org/10.1029/97JB01856

Rave, W., Fabian, K., & Hubert, A. (1998). Magnetic states of small cubic particles with uniaxial anisotropy. *Journal of Magnetism and Magnetic Materials*, *190*(3), 332–348. https://doi.org/10.1016/S0304-8853(98)00328-X

Roberts, A. P., Almeida, T. P., Church, N. S., Harrison, R. J., Heslop, D., Li, Y., et al. (2017). Resolving the origin of pseudo-single domain magnetic behavior. *Journal of Geophysical Research: Solid Earth*, *122*, 9534–9558. https://doi.org/10.1002/2017JB014860

Sahu, S., & Moskowitz, B. M. (1995). Thermal dependence of magnetocrystalline anisotropy and magnetostriction constants of single crystal $Fe_{2.4}Ti_{0.61}O_4$. *Geophysical Research Letters*, *22*(4), 449–452. https://doi.org/10.1029/94GL03296

Shaar, R., & Feinberg, J. M. (2013). Rock magnetic properties of dendrites: Insights from MFM imaging and implications for paleomagnetic studies. *Geochemistry, Geophysics, Geosystems*, *14*, 407–421. https://doi.org/10.1002/ggge.20053

Soffel, H. (1971). The single domain-multidomain transition in natural intermediate titanomagnetites. *Journal of Geophysics*, *37*, 451–470.

Soffel, H. C. (1977). Domain structure of titanomagnetites and its variation with temperature. *Journal of Geomagnetism and Geoelectricity*, *29*(4), 277–284. https://doi.org/10.5636/jgg.29.277

Soffel, H. C., Aumüller, C., Hoffmann, V., & Appel, E. (1990). Three-dimensional domain observations of magnetite and titanomagnetites using the dried colloid SEM method. *Physics of the Earth and Planetary Interiors*, *65*(1-2), 43–53. https://doi.org/10.1016/0031-9201(90)90074-8

Syono, Y. (1965). Magnetocrystalline anisotropy and magnetostriction of $Fe_3O_4$-$Fe_2TiO_4$ series, with special application to rock magnetism. *Japanese Journal of Geophysics*, *4*, 71–143.

Williams, W., Muxworthy, A. R., & Paterson, G. A. (2006). Configurational anisotropy in single-domain and pseudosingle-domain grains of magnetite. *Journal of Geophysical Research*, *111*, B12S13. https://doi.org/10.1029/2006JB004556

Williams, W., & Wright, T. M. (1998). High-resolution micromagnetic models of fine grains of magnetite. *Journal of Geophysical Research*, *103*(B12), 30,537–30,550. https://doi.org/10.1029/98JB01120

Worm, H.-U., & Markert, H. (1987). The preparation of dispersed titanomagnetite particles by the glass-ceramic method. *Physics of the Earth and Planetary Interiors*, *46*(1–3), 263–269. https://doi.org/10.1016/0031-9201(87)90189-0

Xu, S., & Dunlop, D. J. (1996). Micromagnetic modeling of Bloch wall with Néel caps in magnetite. *Geophysical Research Letters*, *23*, 2819–2822.